July 2008
SLAC-PUB-13332
Submitted to ApJ

Discovery of a Giant Lyα Emitter Near the Reionization Epoch [1,2]

Masami Ouchi [3,4], Yoshiaki Ono [5], Eiichi Egami [6], Tomoki Saito [7], Masamune Oguri [8], Patrick J. McCarthy [3], Duncan Farrah [9,10], Nobunari Kashikawa [11], Ivelina Momcheva [3], Kazuhiro Shimasaku [5], Kouichiro Nakanishi [12], Hisanori Furusawa [13], Masayuki Akiyama [14], James S. Dunlop [15,16], Angela M. J. Mortier [16], Sadanori Okamura [5], Masao Hayashi [5], Michele Cirasuolo [16], Alan Dressler [3], Masanori Iye [11], Matt. J. Jarvis [17], Tadayuki Kodama [11], Crystal L. Martin [18], Ross J. McLure [16], Kouji Ohta [19], Toru Yamada [14], Michitoshi Yoshida [20]

Work supported in part by US Department of Energy contract DE-AC02-76SF00515

ABSTRACT

---

[1] Based in part on data collected at Subaru Telescope, which is operated by the National Astronomical Observatory of Japan.

[2] Some of the data presented herein were obtained at the W.M. Keck Observatory, which is operated as a scientific partnership among the California Institute of Technology, the University of California and the National Aeronautics and Space Administration. The Observatory was made possible by the generous financial support of the W.M. Keck Foundation.

[3] Observatories of the Carnegie Institution of Washington, 813 Santa Barbara St., Pasadena, CA 91101

[4] Carnegie Fellow; ouchi _at_ ociw.edu

[5] Department of Astronomy, School of Science, University of Tokyo, Tokyo 113-0033, Japan

[6] Department of Astronomy, University of Arizona, 933 N Cherry Avenue, Rm. N204, Tucson, AZ 85721-0065

[7] Research Center for Space and Cosmic Evolution, Ehime University, 2-5 Bunkyo-cho, Matsuyama 790-8577, Japan

[8] Kavli Institute for Particle Astrophysics and Cosmology, Stanford University, 2575 Sand Hill Road, Menlo Park, CA 94025

[9] Department of Astronomy, Cornell University, Ithaca, NY 14853

[10] Astronomy Centre, University of Sussex, Falmer, Brighton, UK

[11] Optical and Infrared Astronomy Division, National Astronomical Observatory, Mitaka, Tokyo 181-8588, Japan

[12] Nobeyama Radio Observatory, Minamimaki, Minamisaku, Nagano 384-1305, Japan

[13] Subaru Telescope, National Astronomical Observatory of Japan, 650 North A'ohoku Place, Hilo, HI 96720

[14] Astronomical Institute, Graduate School of Science, Tohoku University, Aramaki, Aoba, Sendai 980-8578, Japan

[15] Department of Physics and Astronomy, University of British Columbia, 6224 Agricultural Road, Vancouver V6T 1Z1, Canada

[16] SUPA Institute for Astronomy, University of Edinburgh, Royal Observatory, Edinburgh EH9 3HJ, UK

[17] Centre for Astrophysics, Science & Technology Research Institute, University of Hertfordshire, Hatfield AL10 9AB, UK

[18] Department of Physics, University of California, Santa Barbara, CA 93106

[19] Department of Astronomy, Kyoto University, Kyoto 606-8502, Japan

[20] Okayama Astrophysical Observatory, National Astronomical Observatory, Kamogata, Okayama 719-0232, Japan

We report the discovery of a giant Lyα emitter (LAE) with a Spitzer/IRAC counterpart near the reionization epoch at $z = 6.595$. The giant LAE is found from the extensive 1 deg^2 Subaru narrow-band survey for $z = 6.6$ LAEs in the Subaru/XMM-Newton Deep Survey (SXDS) field, and subsequently identified by deep spectroscopy of Keck/DEIMOS and Magellan/IMACS. Among our 207 LAE candidates, this LAE is not only the brightest narrow-band object with $L(\mathrm{Ly}\alpha) = 3.9 \pm 0.2 \times 10^{43}$ erg s^{-1} in our survey volume of 10^6 Mpc^3, but also a spatially extended Lyα nebula with the largest isophotal area whose major axis is at least $\simeq 3''$. This object is more likely to be a large Lyα nebula with a size of $\gtrsim$ 17-kpc than to be a strongly-lensed galaxy by a foreground object. Our Keck spectrum with medium-high spectral and spatial resolutions suggests that the velocity width is $v_{\mathrm{FWHM}} = 251 \pm 21$ km s^{-1}, and that the line-center velocity changes by $\simeq 60$ km s^{-1} in a 10-kpc range. The stellar mass and star-formation rate are estimated to be $0.9 - 5.0 \times 10^{10} M_\odot$ and $> 34\ M_\odot$yr^{-1}, respectively, from the combination of deep optical to infrared images of Subaru, UKIDSS-Ultra Deep Survey, and Spitzer/IRAC. Although the nature of this object is not yet clearly understood, this could be an important object for studying cooling clouds accreting onto a massive halo, or forming-massive galaxies with significant outflows contributing to cosmic reionization and metal enrichment of inter-galactic medium.

Subject headings: galaxies: formation — galaxies: high-redshift — cosmology: observations

1. Introduction

Identifying the first stage of galaxy formation is one of the ultimate goals in astronomy today. Theoretical models predict that primordial gas accretes onto the center of halo via gravitational cooling with subsequent star-formation activity (Fardal et al. 2001; Yang et al. 2006). These primordial galaxies make spatially extended Lyα nebulae caused by hydrogen cooling, and it is suggested that high-z extended Lyα sources, or Lyα blobs, are candidates for primordial galaxies (e.g. Matsuda et al. 2004; Saito et al. 2006; Nilsson et al. 2006; Smith & Jarvis 2007). Lyα blobs are found mostly at $z \simeq 2 - 3$, and have angular extents of $\simeq 5 - 16$ arcsec with total Lyα luminosities ranging from $\simeq 6 \times 10^{42}$ to 10^{44} erg s^{-1} (Matsuda et al. 2004). The most prominent Lyα nebulae known to date are blobs 1 and 2 found by Steidel et al. (2000), which extend over $\gtrsim$ 100 kpc with $L(Ly\alpha) \simeq 10^{44}$ erg s^{-1}. Although Lyα blobs are candidates for galaxies with gas inflow of cooling accretion, it is also suggested that Lyα blobs can be produced by intensive starbursts associated with significant outflows (e.g., Taniguchi & Shioya 2000; Wilman et al. 2005), by a hidden AGN (e.g., Haiman & Rees 2001), or by both of them (e.g., Dey et al. 2005; Yang et al. in preparation). In fact, the infrared-submm and X-ray observations indicate that Steidel et al.'s blobs 1 and 2 would be powered by a heavily obscured starburst (Geach et al. 2007; Matsuda et al. 2007; see also Chapman et al. 2004) and an AGN (Basu-Zych & Scharf 2004), respectively. Matsuda et al. (2006) claim that all of their spectroscopically-identified Lyα blobs are likely to be the sites of massive galaxy formation because of their large line widths of $v_{\rm FHWM} \gtrsim 500$ km s^{-1}. It is also well known that such bright large Lyα nebulae are associated with radio-loud AGN (e.g. McCarthy et al. 1987; van Ojik et al. 1997; Reuland et al. 2003; Eugenio Barrio et al. 2008) or radio-quit quasars (Weidinger et al. 2005; Hennawi et al. 2008). In this way, extended Lyα nebulae shed light not only on primordial galaxies but also on massive-galaxy formation and AGN activities.

The present studies of extended Lyα nebulae are limited to $z = 2 - 5$ with the majority at $z \simeq 2 - 3$ (e.g., Saito et al. 2008). Due to this redshift limit, it is difficult to identify primordial galaxies as well as to study the early stage of massive galaxy formation. At $z \simeq 2 - 3$, the mean metallicity of the inter-stellar medium is already as high as $Z = 0.1 Z_\odot$ (Sadat et al. 2001; see also Pettini et al. 1997). It is predicted that the fraction of primordial galaxies to metal enriched galaxies would be quite low at $z \simeq 2 - 3$ (Scannapieco et al. 2003), and that the fraction of population III to population II star-formation rate (SFR) rises with increasing redshift (Trac & Cen 2007). On the other hand, the importance of the early stage of massive-galaxy formation has been recognized by the downsizing behavior of stellar-mass assembly (Cowie et al. 1996). A massive population at $z = 2 - 3$ selected from a distant-red galaxy sample is old, $2 - 3$ Gyr, and their mean formation redshift is estimated to be $z \gtrsim 5$ (Labbé et al. 2005; see also Kriek et al. 2006). It is implied that galaxies at the massive end would have a very high specific star-formation rate (SSFR) at $z \gtrsim 4$ (Drory & Alvarez 2008), and that a major active star-formation in massive galaxies probably takes place at $z \gtrsim 4$. Thus, it is important to study extended Lyα nebulae at a redshift greater than the current-observational limit, especially at the reionization epoch of $z \simeq 6 - 11$ (Fan et al. 2006; Komatsu et al. 2008). This epoch is also the today's observational limit of normal star-forming galaxy studies (Iye et al. 2006; Stark et al. 2007; Ota et al. 2008; Bouwens et al. 2008). Moreover, such bright Lyα sources can be a good laboratory for understanding reionization (e.g. Kashikawa et al. 2006; Dijkstra et al. 2007b; McQuinn et al. 2007; Kobayashi et al. 2007) and metal enrichment (e.g. Martin et al. 2002; Bouché et al. 2007) of inter-galactic medium (IGM).

In this paper, we report our discovery of an extended Lyα nebula, which we named Himiko, near the reionization epoch at z=6.595. We describe the photometric identification and spectroscopic confirmation of this object in §2, and present detailed properties such as kinematics and stellar population in §3. We discuss the nature of this object and prospects of future observations in §4. Throughout this paper, magnitudes are in the AB system. We adopt $(h, \Omega_m, \Omega_\Lambda, n_s, \sigma_8) = (0.7, 0.3, 0.7, 1.0, 0.8)$.

2. Discovery

2.1. Photometric Identification

We have identified a candidate very bright spatially-extended Lyα emitter (LAE) at $z \simeq 6.6$ in the course of our deep and wide-field narrow-band imaging program in the Subaru/XMM-Newton Deep Survey (SXDS) field (Ouchi et al. 2008). In 2005-2007, we took narrow-band images in the $NB921$ filter with a central wavelength of $\lambda_c = 9196$Å and a FWHM of 132Å (Hayashino et al. 2003) using Subaru/Suprime-Cam (Miyazaki et al. 2002). The 1 deg^2 field is covered by 5 pointings of Suprime-Cam with a total on-source integration of 45.1 hours. These data are reduced with SDFRED (Yagi et al. 2002; Ouchi et al. 2004), and aligned with optical broad-band images of SXDS (Furusawa et al. 2008). The FWHM of the seeing size in the aligned images is $\simeq 0''.8$. The 3σ limiting magnitude in $NB921$ is $26.2 - 26.4$ mag in a $2''.0$-diameter aperture. Combining the deep optical broad-band images of SXDS, we have selected candidates of $z \simeq 6.56 \pm 0.05$ LAEs that satisfy our photometric criteria of the narrow-band excess ($z' - NB921 > 1.0$), no detection of blue continuum flux ($B > B_{2\sigma}$ and $V > V_{2\sigma}$), and the existence of Gunn-Peterson trough ($[z' < z'_{3\sigma}$ & $i' - z' > 1.3]$ or $[z' \geq z'_{3\sigma}]$). The $B_{2\sigma}$ and $V_{2\sigma}$ are defined as 2σ limiting magnitudes of B and V bands, respectively ($B_{2\sigma} = 28.7$ and $V_{2\sigma} = 28.2$), while $z'_{3\sigma}$ is the 3σ detection limit ($z'_{3\sigma} = 26.5$). We have obtained a photometric sample of 207 LAEs at $z \simeq 6.6$ down to $NB921 = 26.0$ in a comoving survey volume of 8×10^5 Mpc^3. The sky distribution of our LAEs show a rectangular area ($8' \times 20'$) with a number density of LAEs higher than the average by a factor of 2. In this high-density region, we find the object, Himiko, (R.A.$= 2^h17^m57.563^s$, decl.$= -5°08'44.45''$ [J2000]) [1] that has the brightest $NB921$ magnitude and the largest isophotal area among the 207 LAE candidates. The total magnitude of Himiko is $NB921 = 23.55$, which is brighter than the second brightest candidate ($NB921 = 24.06$) by 0.5 magnitude. This object is significantly extended, in contrast to the compact point-like profiles of the other LAEs. If we define the isophotal area, $A_{\rm iso}$, as pixels with values above the 2σ sky fluctuation (26.8 mag arcsec^{-2} in $NB921$), the isophotal area of Himiko is $A_{\rm iso} = 5.22$ arcsec^2 in the $NB921$ image. Figure 1 presents

---

[1] Based on SXDS ver1.0 astrometry (Furusawa et al. 2008).

the isophotal area of our $z = 6.6$ LAE candidates as a function of total $NB921$ magnitude and average $NB921$ surface brightness. The average $NB921$ surface brightness, $\langle SB \rangle$, is the value of an isophotal flux divided by the isophotal area, where the isophotal flux is the one summed over the isophotal area. We mark a possibly extended (FWHM$> 1''.2$) sources with a filled squares to distinguish between bright point-like and faint extended sources with a comparable isophotal area. Figure 1 indicates that there are no LAEs similar to Himiko. We confirm that the brightest source from the previous 0.2 deg^2 Subaru Deep Field (SDF) survey for $z \sim 6.5$ LAEs is only as bright as our second brightest candidate with no significant spatial extent (Taniguchi et al. 2005; Kashikawa et al. 2006), and that our object is distinguished from all the other $z \sim 6.5$ LAEs found in the previous studies. We present snapshot images in Figure 2 and a close-up color composite image in Figure 3. The major axes of the isophotal area in $NB921$ and z' bands are $\simeq 3''.1$ and $\simeq 2''.0$, respectively. Additionally, the $NB921$ (z') image shows potential diffuse components which continuously extend by $\sim 1''$ ($\sim 0''.3$) around the isophotal area with a surface brightness above 1σ sky fluctuation (Figures 2 and 3). Thus, the size of our object is probably $\gtrsim 3''.1$ and $\gtrsim 2''.0$ in $NB921$ and z' bands, respectively. Given the fact that this LAE has the unusual brightness and size, we refer to this object as the giant LAE.

Interestingly, this object is detected at the 4σ level in the medium deep 3.6μm image from the Spitzer legacy survey of the Ultra Deep Survey field (SpUDS; PI:. J. Dunlop; Figure 2), while we find only marginal detections ($\sim 2 - 3\sigma$) [2] in the near-infrared (NIR) images from the UKIRT Infrared Deep Sky Survey Third Data Release (UKIDSS-DR3: Lawrence et al. 2007). We align Spitzer/SpUDS and UKIDSS-DR3 images with the SXDS optical images, referring a number of stellar objects in the field. The relative astrometric errors are estimated to be $\simeq 0''.04$, $\simeq 0''.11$, and $\simeq 0''.35$ in rms, for optical-NIR, Spitzer/IRAC($3.6-8.0\mu$m), and MIPS(24μm) images, respectively. We summarize total magnitudes/fluxes and $2''$-diameter aperture magnitudes of Himiko in Table 1. We define the total magnitude with MAG_AUTO of SExtractor (Bertin & Arnouts 1996) in the optical and NIR bands. The total magnitudes of Spitzer/IRAC and MIPS bands are obtained from a $3''$-diameter aperture and an aperture correction given in Yan et al. (2005) and the MIPS web page [3], respectively. Note that our object is detected in the 3.6μm band, but not in the 4.5μm band. This is probably due to the higher noise level in the 4.5μm band, as we expect the object to have a fairly flat spectrum at these wavelengths. Our measured 3.6μm magnitude of 24.02 (4σ) would result in a $< 3\sigma$ detection at 4.5μm for a flat spectrum (constant AB magnitude), consistent with

---

[2] We estimate the 2σ limits of total magnitudes in the vicinity of this object to be $J = 24.3$, $H = 24.0$, and $K = 23.8$.

[3] http://ssc.spitzer.caltech.edu/mips/apercorr/

our tentative $1-2\sigma$ detection and the large error with 24.62 ± 0.73 [4].

2.2. Spectroscopic Confirmation

We carried out spectroscopic follow-up observations with Keck/DEIMOS and Magellan/IMACS. The DEIMOS observations were conducted with the 830G grating and the GG495 filter in the non-photometric night on 2007 November 5. The IMACS observations were made in the nod-and-shuffle mode with the 150 l mm^{-1} grism and the GG455 filter under the photometric night on 2007 November 11. The on-source exposure times of our DEIMOS and IMACS observations were 10800 and 15600 seconds in the $0''.8-1''.0$ and $0''.5-0''.8$ seeing conditions, respectively. We chose $1''.0$ for the slit width in these observations. The DEIMOS slit position is plotted in Figure 2. The slit position of IMACS is the same as that of DEIMOS, but the position angle is slightly rotated by -1.1 deg. The spectral coverages of DEIMOS and IMACS are $5700-9500$Å and $4500-9700$Å, respectively. The spectral resolution of the DEIMOS data at 9200Å is $R\simeq3600$, while the one of the IMACS data is $R\simeq700$. We have reduced our spectra with spec2d [5] and COSMOS pipelines for DEIMOS and IMACS data, respectively. Both spectra have a strong single line with no detectable continuum. The line-center wavelength of the single line is 9232.7Å from our DEIMOS spectrum, which coincides with the measurement from our IMACS spectrum (9233.5Å) within 1Å. Figure 4 presents our spectra in the wavelength around this single line. We have confirmed that the spectra show no signatures of an [OIII] 5007 emission line (at $\simeq 7044$Å) and an [OII] 3727 emission line (at $\simeq 5243$Å) from a $z=0.407$ Hα emitter or an [OII] emission line (at $\simeq 6872$Å) from a $z=0.844$ [OIII] emitter, and found that this object is neither a foreground Hα nor [OIII] emitter. We cannot distinguish between an [OII] emitter at $z=1.477$ and a Lyα emitter at $z=6.595$ from a detection of the other emission line, because our spectra do not cover a wavelength that would have another strong emission line such as Lyα, [OII], [OIII], and Hα. However, the DEIMOS spectrum has a FWHM spectral resolution of 2.6Å that would have enabled us to identify an [OII] $\lambda\lambda$3726,3729 doublet at $z=1.48$ with a separation of 6.9Å (vertical arrows in the middle panel of Figure 4). Our DEIMOS spectrum confirms no such signature of [OII] doublet, but a clear asymmetric line profile with an extended red wing that is typical for a high-z Lyα line. We measure the skewness, S, and the weighted skewness, S_w, defined by Kashikawa et al. (2006). We obtain

---

[4] See §3.1 for a possible inclusion of emission lines in the IRAC bands.

[5] The analysis pipeline used to reduce the DEIMOS data was developed at UC Berkeley with support from NSF grant AST-0071048.

$S = 0.685 \pm 0.007$ and $S_w = 13.2 \pm 0.1$ for our line. Since the average values of $z \sim 6.5$ LAEs are $S = 0.542 \pm 0.007$ and $S_w = 11.5 \pm 0.2$ (Kashikawa et al. 2006), the line shape of our object is similar to (or more positively skewed than) the average. If this line were an [OII] doublet, the line shape would be negatively skewed. Thus, we conclude that this object is a real LAE at $z = 6.595$ with a clear red wing in the asymmetric Lyα line. This is the spectroscopic confirmation of the giant LAE, Himiko, at $z = 6.595$. The number density corresponding to this object is only 1.2×10^{-6} comoving Mpc^{-3} at $z = 6.6$ We have identified the rare object near the reionization epoch.

We estimate Lyα flux, $f(\mathrm{Ly}\alpha)$, and rest-frame equivalent width, EW_0, to be $f(\mathrm{Ly}\alpha) = 7.9 \pm 0.5 \times 10^{-17}$ erg s^{-1} cm^{-2} and $EW_0 = 100^{+302}_{-43}$ Å with z' and $NB921$-band photometry in the same manner as Ouchi et al. (2008). The corresponding Lyα luminosity, $L(\mathrm{Ly}\alpha)$, is $L(\mathrm{Ly}\alpha) = 3.9 \pm 0.2 \times 10^{43}$ erg s^{-1}. To check our estimation, we derive $f(\mathrm{Ly}\alpha)$ from the IMACS spectrum that were taken under the photometric condition. Applying a slit-loss correction, we obtain $f(\mathrm{Ly}\alpha) = 11.2 \pm 3.6 \times 10^{-17}$ erg s^{-1} cm^{-2} corresponding to $L(\mathrm{Ly}\alpha) = 5.6 \pm 1.8 \times 10^{43}$ erg s^{-1}. Although the line-flux value from the IMACS spectrum includes the large error, the line flux from spectroscopy agrees with the one from photometry within the 1σ error. Since the IMACS spectrum shows no continuum above the detection limit, EW_0 cannot be derived from the spectrum. We summarize spectroscopic as well as various properties of this object in Table 2.

3. A Giant LAE at $z = 6.595$

3.1. AGN Activity

If this object is an AGN, strong [OIII] and Hα emission lines would enter into the 3.6μm and 4.5μm bands, respectively, which would boost the magnitudes in these bands. We estimate the possible contributions from these strong lines, assuming the flux ratios of $f_{\mathrm{Ly}\alpha}/f_{[\mathrm{OIII}]} = 4$ for a type II AGN (McCarthy 1993; see below for the reason of type II) and $f_{\mathrm{Ly}\alpha}/f_{\mathrm{H}\alpha} = 8.7$ for the case B recombination (Brocklehurst 1971). We, thus, obtain 26.3 and 27.0 magnitudes in 3.6μm and 4.5μm bands, respectively. Since the magnitude of our object is 24.0 in the 3.6μm band, the flux contributed from strong lines of AGN would be about one-order of magnitude smaller than the brightness of our object. Even with an AGN, the magnitudes of 3.6μm and 4.5μm bands would include a negligible contribution from strong emission lines. It should be noted that these flux contributions from strong lines could be underestimated, in the case where our Lyα flux is very strongly absorbed.

We investigate the AGN activity in our object. Our spectra show no NV 1240 line at

9418Å as well as no broadening of Lyα. Moreover, there is no counterpart in our MIPS image as well as the X-ray and radio catalogs (Ueda et al. 2008; Simpson et al. 2006) whose detection limits are $m(24\mu\text{m}) = 19.8$, $f(0.5 - 2\text{keV}) = 6 \times 10^{-16}$ erg cm^{-2} s^{-1}, and $f(1.4\text{GHz}) = 100\mu\text{Jy}$, respectively. Our object is not also detected in the SCUBA Half-Degree Extragalactic Survey (SHADS; Mortier et al. 2005) data. We find no significant signal at the location of our object in the submm 850μm map, and obtain the 3σ upper limit flux of $S(850\mu m) < 12$ mJy. Although these constraints of AGN are weak, there are no obvious signatures of AGN activities.

3.2. Possibility of Gravitational Lensing

Because the source is extended, we have investigated the possibility of gravitational lensing by a foreground object. First, we use the catalog of van Breukelen et al. (2006) which shows cluster candidates at $z = 0.5 - 1.5$ in this field. The estimated masses of these clusters range between $5 \times 10^{13} - 3 \times 10^{14} M_{\odot}$. Our object is separated from the center of the closest cluster candidate by $\simeq 5'.8$. Due to this large separation, the magnification by these clusters is negligible.

Next, we investigate the possibility of galaxy-galaxy lensing. Figure 2 indicates that this source may have two peaks in the z' image, and a smooth profile in the $NB921$ image. From a visual inspection, the 3.6μm-band profile would appear to be slightly elongated. However, our object is not bright enough in the 3.6μm band to distinguish between profiles of a real extended source and a point source with outskirts made by peaks of background fluctuations. We carry out profile fitting to our z' and $NB921$ images with GALFIT (Peng et al. 2002). We fit two profiles whose flux amplitudes and positions are free parameters. We find that fitting with two PSF profiles leaves large residuals, and that the profile of our object is well fit by two circular exponential disks with a half-light radius of $R_{\text{hl}} = 0''.3$ which are separated by $1''.1$. The positions of two components are determined in the z'-band image that shows the possible two peaks, and presented with green arrows in Figure 2. On the other hand, the two-exponential disk models can reproduce not only the z'-band, but also the $NB921$-band profiles. The positions of the best-fit models in the $NB921$ image are not the same as those in the z' image, but the differences of the positions are only $0''.2 - 0''.3$. Because the photometric uncertainties in the z' band are large, it is not clear whether two peaks really exist or whether the positions of two peaks are different between the z' and $NB921$ images. Nevertheless, we refer to the positions of east and west components determined in the z' image as *position* 1 and 2, respectively. The brightness ratio, Δm, of *position* 1 (m_1) and 2 (m_2) components are $\Delta m \equiv m_2 - m_1 = 0.38 \pm 0.38$ and 0.65 ± 0.10 in z' and $NB921$ bands, respectively. There are no significant differences between Δm of z' and $NB921$ bands. We cannot reject the possibility that these two components have the same color, and that these components are an identical lensed object. Thus, our profile fitting does not constrain the possibility of lensing due to the large photometric uncertainties of Δm.

Figure 5 presents DEIMOS spectra at *position* 1 and 2 whose extraction-aperture size is $0''.6$ along the slit. The skewness and the weighted skewness of the emission line are estimated to be $(S, S_w) = (0.846 \pm 0.018, 17.3 \pm 0.4)$ and $(0.502 \pm 0.023, 9.3 \pm 0.4)$ in the spectra at (*position* 1, *position* 2). These two spectra show an asymmetric line with S and S_w which are comparable with the average values of $z \sim 6.5$ LAE (see §2.2). Thus, both of these components reside at high-z. The bottom panel of Figure 5 presents line-center offset and line width as a function of distance along the DEIMOS slit. We measure the line center and width by Gaussian-profile fitting. Note that the $NB921$ (or Lyα) surface-brightness distribution is not homogeneous within the slit. In fact, Figure 2 implies that, from *position* 1 to 2, the profile center would shift towards the direction of red spectrum (magenta arrows in Figure 2). We estimate the biases raised by this profile inhomogeneity with the $NB921$ image which has a seeing size comparable to our DEIMOS spectrum. We measure changes of the profile's center and standard deviation within the slit as a function of slit position in the $NB921$ image. We calculate the correction factors in wavelength based on these spatial changes of $NB921$ profile, and apply these correction factors to the original measurements of line-center offset and line width. The bottom panel of Figure 5 shows the corrected values (filled squares), together with the original measurements (open squares). We confirm that those biases are not large enough to alter general trends in line-center offset and line width. Figure 5 indicates that the Lyα-line center shifts gradually by $\simeq 30$ km s^{-1} between these two components. Thus, these components are not sources of an identical object produced by lensing because of this line shift. It indicates that it is unlikely that they are gravitationally lensed objects. Moreover, following the method introduced in §2.4.2 of Pindor et al. (2006), we estimate the minimum brightness of lensing galaxy at $z < 4$ to be $K = 23.2$ based on our source redshift of 6.6 and image separation of $1''.1$. Figure 2 presents no nearby bright sources with $K \lesssim 23.2$ to which can be ascribed a lensing object. There remains a special case where a very red foreground object with a 3.6μm-band detection and no optical-NIR counterparts magnifies an inhomogeneous LAE with spatially different magnification factors. However, there are little chance coincidences in the precise alignment of such an extremely-red lensing object. We thus conclude that our LAE is not likely to be a lensed source, but an intrinsically extended object. The size of the extended Lyα nebula is $\gtrsim 17$ proper kpc at $z = 6.595$ which is estimated from the major axis of the isophotal area in the $NB921$ image ($\gtrsim 3''.1$; §2.1).

3.3. Kinematics of Resonance Lyα Line

Because Lyα is a resonance line strongly scattered or absorbed by gas and dust, it is difficult to determine the gas kinematics by Lyα observations alone. However, it is known that Lyα line is a useful probe of gas inflow/outflow and cosmic reionization with detailed modeling (Tapken et al. 2007; Dijkstra et al. 2007a). First, we obtain the line width of $v_{\rm FWHM} = 251 \pm 21$ km s^{-1} from the DEIMOS spectrum in the extraction aperture of $1''.2 \times 1''.0$ (i.e. 6.5×5.4 proper kpc^2) around the Lyα source center which corresponds to $\Delta d = 0$ in Figure 5. The line width is corrected for the instrumental broadening with the assumption of a Gaussian profile. The line width can be twice as large as this value, if a blue half of Lyα is completely absorbed by IGM with no effects of the Lyα damping wing. From further inspection of the line-center offset and line width along our DEIMOS slit (Figure 5), we find that the line-center velocity of Lyα increases by $\Delta v \simeq 60$ km s^{-1} from east to west in a range of $\sim 2''$ ($D = 10$ proper kpc). Note that this small velocity offset is larger than the sizes of their error bars. [6] On the other hand, there are no significant changes of line width beyond the sizes of their error bars, although our spectrum implies an increase by ~ 50 km s^{-1} from east to west.

3.4. Stellar Population and Mass

We carry out χ^2 fitting of stellar synthesis models to the spectral energy distribution (SED) of this object based on total fluxes at the observed-frame of $0.9 - 8.0\mu$ m (Table 1). Since our z'-band photometry is contaminated by Lyα emission and Gunn-Peterson trough, we estimate the emission-free continuum magnitude at 9500Å, $m_{0.95}$. We obtain $m_{0.95} = 25.18 \pm 0.73$ based on $NB921$- and z'-band photometry by the method similar to that of Shimasaku et al. (2006), which takes account the contributions of the Lyα line and IGM absorption (Madau 1995) with the response curves of $NB921$ and z' filters. We use the stellar synthesis models of Bruzual & Charlot (2003) with dust attenuation of Calzetti et al. (2000). Applying models of constant and exponentially-decaying star-formation histories with sets of metallicity in $Z = 0.02 - 1.0 Z_\odot$, we search for the best-fit model in a parameter space of $E(B-V) = 0 - 1$ and age$= 1 - 810$ Myr, where the upper limit of stellar age is the cosmic age at $z = 6.595$. First, we assume the constant star-formation with a fixed metallicity of $Z = 0.02 Z_\odot$. Figure 6 presents the SED and the best-fit models. We find that

---

[6] Although the instrumental spectral resolution is $R \sim 3600$ corresponding to $v_{\rm FWHM} \sim 80$ km s^{-1}, the uncertainties of line centering by Gaussian fitting is as small as $\sim 5 - 10$ km s^{-1} (See error bars in Figure 5).

the best-fit model has a stellar mass of $M_* = 3.5^{+1.5}_{-2.6} \times 10^{10} M_\odot$ (i.e. $0.9 - 5.0 \times 10^{10} M_\odot$) with a reduced χ^2 of 0.84. Because very weak photometric constraints are given in the rest-frame near UV ($\sim 0.2 - 0.3 \mu$m) critical to resolving the degeneracy between extinction and age, we obtain no meaningful measurements on extinction and stellar age within the $\simeq 1\sigma$ error. For examples, the sets of allowed parameters are (E[B-V], age[Myr])= $(0.0, 810)$, $(0.3, 200)$, $(0.6, 29)$, and $(0.9, 3)$. On the other hand, our estimate of stellar mass ($0.9 - 5.0 \times 10^{10} M_\odot$) has a moderate reliability due to the determinations of precise spectroscopic redshift and the rest-frame optical photometry on which stellar mass primarily depends. It should be noted that this object is the most distant spectroscopically-confirmed galaxy whose stellar mass is constrained. Next, we change the metallicity to $Z = 0.2 - 1.0 Z_\odot$ and star-formation history to an exponential-decay time scale of $\tau = 1 - 100$ Myr. The stellar mass is estimated to be $1.7 - 3.2 \times 10^{10} M_\odot$ and $0.4 - 4.8 \times 10^{10} M_\odot$ for the best-fit values and the 1σ error ranges, respectively. We find that the general behaviors of the fitting is the same, and that the best-fit values and the 1σ error ranges of stellar mass agree with those from the first assumptions ($0.9 - 5.0 \times 10^{10} M_\odot$) within a factor of $\simeq 2$.

Mobasher et al. (2005) report a very massive galaxy at $z_{\rm phot} = 6.5$ with a stellar mass of $6 \times 10^{11} M_\odot$ based on a photometrically-selected galaxy. However, there are some controversial claims that Mobasher et al.'s object is a low-z starburst from reanalysis of its photo-z (Dunlop et al. 2007) and the detection of polycyclic aromatic hydrocarbon emission features from a $z \sim 2$ object (Chary et al. 2007). On the other hand, Labbé et al. (2006) study z-dropout galaxies with a photo-z of $z \sim 7$ in the Hubble Ultra Deep Field (HUDF), and find that these galaxies have stellar masses of $0.1 - 1 \times 10^{10} M_\odot$. This mass range touches the lowest-mass limit of our object ($0.9 - 5.0 \times 10^{10} M_\odot$). If the Labbé et al.'s photo-z objects are real high-z galaxies, our object is likely to be a more stellar-massive galaxy than those found in the small area of HUDF. Similarly, Egami et al. (2005) have estimated a stellar mass of a gravitationally-lensed galaxy at $z \sim 7$ behind the A2218 cluster to be $\sim 10^9 M_\odot$, which is about an order of magnitude smaller than the stellar mass of our object.

Because $E(B-V)$ cannot be constrained, we can only obtain the lower-limit of star-formation rate of $SFR > 34 M_\odot {\rm yr}^{-1}$ from the SED fitting, which is given in the case of $E(B-V) = 0$. This lower limit from the SED fitting is consistent with the SFRs estimated from the UV continuum of $m_{0.95}$ (SFR=$25^{+24}_{-12} M_\odot$ yr^{-1}) and from the Lyα luminosity (SFR=$36 \pm 2 M_\odot$ yr^{-1}) with no dust-extinction corrections via formulae of Madau, Pozzetti, & Dickinson (1998) and Kennicutt (1998) + case B recombination, respectively.

The SSFR of our object is $SSFR > 1.6 \times 10^{-9} {\rm yr}^{-1}$ at the stellar mass of $0.9 - 5.0 \times 10^{10} M_\odot$. In the plane of SSFR vs. stellar mass, our lower limit of SSFR is comparable to LBGs at $z \simeq 2 - 3$ (see, e.g., Castro Cerón et al. 2008). However, the stellar mass of our object is, at least, one-order of magnitude larger than that of the averaged (stacked) LAEs at $z \sim 3$ (Nilsson et al. 2007; Gawiser et al. 2007; Lai et al. 2008). Our derived stellar mass is more similar to those of luminous LAEs at $z = 3.1 - 5.7$ that are bright enough to be identified individually in infrared images (Lai et al. 2007; Finkelstein et al. 2008; Ono et al. in prep; cf. very faint LAEs in the HUDF by Pirzkal et al. 2007).

We calculate four statistical measurements from our object's SFR, stellar mass, and number density listed in Table 2, and compare with those obtained by the other studies. The comparisons are useful to check how our object plays a role in the average volume of the Universe at $z \sim 7$. (i) We estimate the lower limit of UV luminosity function (LF) to be $\gtrsim 1.2 \times 10^{-6}$ mag^{-1} Mpc^{-3} at $M_{\rm UV} \simeq -21.3$. This limit is consistent with $z \sim 7$ UV LF of Bouwens et al. (2008). (ii) The lower limit of cosmic SFR is $> 4.3 \times 10^{-5} M_\odot$ yr^{-1} Mpc^{-3}, which is one to two orders of magnitude smaller than that obtained by Bouwens et al. (2008). Thus, this limit is consistent with the estimate of Bouwens et al. (2008). The small contribution to the cosmic SFR leaves the possibility that significantly luminous objects like the one we discuss here could not be the major contributors of cosmic reionization at $z \sim 7$ similar to at $z \sim 6$ (Yan & Windhorst 2004). (iii) The lower limit of stellar-mass function is $\log \rho_* > -5.9$ Mpc^{-3} dex^{-1} at $\log(M_*) \simeq 10.5$. This limit is much lower than stellar mass function of $z \sim 5$ dropouts given by McLure et al. (2008). It indicates that our lower limit is compatible with the scenario of hierarchical structure formation, because a similarly massive system is more abundant at the recent epoch of $z \sim 5$ than at $z \sim 7$. (iv) The lower limit of stellar-mass density is $> 4.4 \times 10^4 M_\odot$ Mpc^{-3}, which is consistent with that obtained in the HUDF ($1.6 \times 10^6 M_\odot$ Mpc^{-3}; Labbé et al. 2006). All of these four statistical measurements corresponding to our object fit in the average properties of the Universe at $z \sim 7$.

4. Discussion

4.1. Comparisons with Lyα Blobs at $z \sim 3$

We compare properties of our giant LAE with those of Lyα blobs found at $z \simeq 3$. Because objects experience more severe surface-brightness dimming at $z = 6.6$ than at $z \simeq 3$, careful comparisons are needed. We produce simulated $NB921$ images of blob 1 of Steidel et al. (2000) and blob 28 of Matsuda et al. (2004) redshifted to $z = 6.595$ based on the narrow-band images of Matsuda et al. (2004). We choose the blob 1 and 28, because they have the brightest Lyα luminosity and the highest surface brightness, respectively, in Matsuda et al.'s catalog. We carry out the simulations in the same manner as Saito et al. (2006), but with an improved random noise whose amplitude exactly matches to those of real $NB921$ image. Figure 7 presents the simulated $NB921$ images, together with the original narrow-band images of Matsuda et al. (2004). The simulated image of blob 1 indicates that our observations would miss $\simeq$ 95% of blob 1's $L(\mathrm{Ly}\alpha)$, and that no diffuse Lyα nebula could be identified. The simulated blob 1 has ($NB921$[total], A_{iso}, $\langle SB \rangle$) = (25.5 mag, 0.8 arcsec^2, 26.7 mag arcsec^{-2}). We plot this simulated object in Figure 1. The simulated blob 1 is indistinguishable from the cloud of normal LAEs in the planes of A_{iso} vs. $NB921$ and A_{iso} vs. $\langle SB \rangle$. On the other hand, the simulated blob 28 shows ($NB921$[total], A_{iso}, $\langle SB \rangle$) = (24.1 mag, 3.7 arcsec^2, 26.3 mag arcsec^{-2}). This simulated object is recognizable in Figure 1. However, this simulated object is more similar to the other LAEs with the second and third largest A_{iso} than to our object. There exist remarkable differences in A_{iso} and $\langle SB \rangle$ (or $NB921$ magnitude) between our object and the simulated objects. In other words, the large A_{iso} and the high $\langle SB \rangle$ of our object at $z = 6.6$ cannot be realized even for blob 28 whose very high surface brightness would minimize the effect of cosmological surface brightness dimming. It implies that our object might be a population that has not yet been identified at $z \simeq 3$.

Although the Lyα brightness and profile of our object seem different from those of Lyα blobs at $z \simeq 3$, the other properties of our object show both similarities and differences. The line width of our object is comparable to some of the extended LAEs presented in Matsuda et al. (2006) in the plane of FWHM(Lyα) vs. isophotal area, although the threshold of isophotal area is different from ours. On the other hand, there are no objects with such a luminous Lyα line in the range of $v_{\mathrm{FWHM}} = 100 - 900$ km s^{-1} in the catalog of Saito et al. (2008). The velocity width of our object is 251 km s^{-1} which is significantly smaller than that of Steidel et al.'s blob 1 with a broad-velocity width, $\simeq 1000 - 1500$ km s^{-1} (Ohyama et al. 2003; see also Bower et al. 2004). The velocity width of our object is closer to the one of blob 28 ($v_{\mathrm{FWHM}} = 362$ km s^{-1}; Y. Matsuda in preparation). The stellar masses of the sub-components shaping Steidel et al.'s blobs 1 and 2 range from 10^{10} to $10^{11} M_{\odot}$ (Uchimoto et al. 2008), which is comparable to ours. Similarly, Smith et al. (2008) report that the stellar mass of their Lyα blob at $z = 2.83$ is as massive as $3 - 4 \times 10^{11} M_{\odot}$. These stellar masses are comparable to ours within an order of magnitude. The estimated number density of our object is only 1.2×10^{-6} comoving Mpc^{-3}, which is lower than those of $z \sim 3$ Lyα blobs found by Matsuda et al. (2004) (3×10^{-4} Mpc^{-3}), Saito et al. (2006) (1×10^{-5} Mpc^{-3}), and Yang et al. in preparation (3×10^{-6} Mpc^{-3}). This number density is also lower than the upper limit of number density of Steidel et al.'s two Lyα blobs (2×10^{-5} Mpc^{-3}), which are estimated from the number of objects (2) and Matsuda et al.'s survey volume (1.3×10^5 Mpc^3). Although these number densities depend on the criteria of sample selections and observing fields, our object at $z = 6.6$ would be as rare as (or even rarer than) these Lyα blobs at $z \sim 3$. Regarding the environment, our giant LAE resides in a high density region of LAEs (§2.1). Matsuda et al. (2004) find that, at $z = 3.1$, the distribution of their Lyα

blobs trace the dense regions of LAEs. The similar spatial correlation between our extended LAE and compact LAEs is also seen at $z = 6.6$.

4.2. Inferred Kinematics

If this object forms a single virialized system whose possible two z'-band components would be just bright H II regions in a disk (see §4.3), the dynamical mass from the rotation is naively estimated to be $M_{\rm rot}\sin(i) \simeq 1 \times 10^9 M_\odot$ by $M_{\rm rot}\sin(i) = ([v_c \sin(i)]^2 r)/G$ with $v_c \simeq \Delta v/2 = 30$ km s^{-1} and $r = D/2 = 5$ kpc (§3.3), where i and G are the inclination of a rotating disk and the gravitational constant. On the other hand, from the 1-dimensional velocity dispersion of $\sigma_v = v_{\rm FWHM}/2.35 = 107$ km s^{-1} in a half size of the extraction aperture, $R \sim 6/2 = 3$ kpc (§3.3), we obtain the mass of random motion of $M_{\rm rand} = 4 \times 10^{10} M_\odot$ via $M_{\rm rand} = (5/3)(3\sigma_v^2)R/G$, assuming a uniform sphere. If the blue half of Lyα is absorbed by the external IGM, the velocity dispersion and mass are $\simeq 214$ km s^{-1} and $M_{\rm rand} = 2\times10^{11} M_\odot$, respectively. Thus, $M_{\rm rand}$ is 1-2 order(s) of magnitude larger than $M_{\rm rot}$ in a reasonable range of inclination ($i = 10 - 90°$). If we consider the smaller radius for the $M_{\rm rand}$ estimate ($R = 3$ kpc) than that for the $M_{\rm rot}$ estimate ($r = 5$ kpc), the difference of these dynamical masses defined in a common radius becomes even larger. If Lyα reflects dynamics, our giant LAE would be a system more dominated by random motion than rotation. Note that these estimates of dynamical masses depend on the size of spectrum extraction aperture with the uncertainties of seeing smearing, and that these results are only true under the assumptions of the single-virialized system and no significant effects of resonant scattering.

If this giant LAE is an outflow object whose Lyα emission is produced by shock heating (cf. Dijkstra & Loeb 2008), the dynamical time scale required to form the extended Lyα nebula is $\simeq 7 \times 10^7$ yr, where we assume the size of the major axis ($\simeq 17$ kpc) and the typical velocity width ($v_{\rm FWHM} = 251$ km s^{-1}). Since this time scale is as long as the cosmic time between $z = 6.595$ and 7.1, it would start making an ionized-bubble since $z = 7.1$ in this shock heating scenario.

4.3. Nature of the giant LAE

The nature of the Lyα nebula of our object is not yet clearly understood within the currently available observational data. There are five possible explanations: (1) halo gas photoionized by a hidden AGN, (2) clouds of H II regions in a single virialized galaxy, (3) cooling gas accreting onto a massive dark halo associated with an initial onset of starburst at the halo center, (4) merging bright LAEs with clouds of HII regions, and (5) outflowing gas excited by shocks or UV radiation from starbursts and/or mergers. There is a chance of (1), but no positive evidence of an AGN. We find the lack of NV line, no line broadening, and no detections in MIPS, X-ray, submm, and radio bands, although these constraints on a hidden AGN are weak. The case of (2) seems surprising, because it means that such a large galaxy exists in a very early epoch of $z = 6.6$. This galaxy would have a size of $\gtrsim 17$ kpc and possibly two large star-forming regions in a disk seen in our z' band image (§3.2). However, there is a chance to explain this large galaxy in the framework of Cold Dark Matter (CDM) models. We estimate properties of the most massive dark halo whose number density is the same as our object at $z = 6.6$. Based on the analytic CDM model of Sheth & Tormen (1999), we find that the dark halo has a radius of 47 kpc and a mass of $1 \times 10^{12} M_{\odot}$ with a circular velocity of 380 km s^{-1}. All of these values of the dark halo are significantly larger than those of our giant LAE measured via radiation, indicating that the single-galaxy picture can be compatible with the CDM model in terms of halo properties. But it is not obvious that such a big virialized baryonic system at $z = 6.6$ can be reproduced in the scheme of CDM model. The case of (3) is possible with the potentially large EW_0 of $57 - 402$Å. The comparable SFR values from Lyα and UV continuum (§3.4) may not prefer this scenario, since the Lyα luminosity could be explained solely by normal star-forming activities that the UV continuum indicates. However, this argument is not strong due to the underestimation of SFR from Lyα luminosity. In fact, the intrinsic Lyα luminosity could be brighter by a factor of 20 if our giant LAE has diffuse Lyα components similar to Steidel et al.'s blob 1 (§4.1). The explanation of (4) would be reasonable, given the possible existence of two peaks in z' band with a separation of $1''.1$ (6.0 kpc). The $NB921$-image profile can be reproduced by two exponential disks with a reasonably small half-light radius of $R_{\mathrm{hl}} = 0''.3$ corresponding to $R_{\mathrm{hl}} = 1.6$ kpc (§3.2; cf. Simard et al. 1999). The merger would induce star-formation activities, and could produce the bright Lyα-line and UV-continuum emission. Figure 5 shows that velocity widths at *position* 1 and 2 are similar, implying that dynamical masses of these components would be comparable. We may be witnessing the site of a major merger near the reionization epoch. On the other hand, our object shows a Lyα nebula potentially larger than the isophotal scale with the major axis of $3''.1$ (17 kpc; §2.1). If the Lyα nebula really extends beyond the 2σ-level isophotal area, it becomes difficult to explain the Lyα morphology with a profile of two merging LAEs. The (5) case seems plausible, since our object has a relatively high SFR and a large stellar-mass with possible multiple components in z' band (§3.2). In either case of (4) or (5), our object would be a massive galaxy in formation with significant star-formation contributing to cosmic reionization (cf. Iliev et al. 2006) and/or with outflows for the metal enrichment of IGM (Bouché et al. 2007). Since our object has the small velocity offset ($\Delta v = 60$km s^{-1}) and the line width ($v_{\mathrm{FWHM}} = 251$ km s^{-1}), the dynamics of merger or outflow would have to be well collimated to the direction perpendicular to the line of sight.

The angular size of the Lyα nebula is $\gtrsim 17$ proper kpc (§3.2), which is comparable to the diameter of the stellar disk of the present-day Milky Way. It is impressive, if we consider that the age of the Universe at $z = 6.595$ is only 6% of the one of the present-day Universe. Moreover, such an extended Lyα source is very rare in the cosmological volume only with the number density of 1.2×10^{-6} comoving Mpc^{-3} at $z = 6.6$ (§2.2). If our selection of large Lyα nebula does not miss a significant fraction of massive galaxies at this early epoch ($z = 6.6$), our object could be an ancestor of a bright-cluster or cD galaxy, and should be a good laboratory of massive-galaxy formation near the reionization epoch.

4.4. Future Prospects

The currently available data do not provide a clear answer to the question about the nature of this object. It is obvious that deeper NIR and infrared images of this object can be taken with Hubble and Spitzer Space Telescopes to constrain dust extinction, SFR, and stellar age, which will trace back through the star-formation history of this object (e.g. Yan et al. 2006; Eyles et al. 2007). More importantly, we can characterize star-formation activities and metal enrichment in our Lyα nebula by deep submillimeter and millimeter observations with Atacama Large Millimeter/Submillimeter Array (ALMA) which will start the operation in 2012 preceded by the early-science operation. ALMA observations will allow us to investigate emission from dust and molecular-clouds in our object. Submm observations would provide an independent probe of SFR that is useful to identify Lyα photons that are not originated from star-formation activities but from the others, such as cold accretion. A detection of spatially-extended metal line from the Lyα nebula could reject the possibility of cooling accretion of primordial gas.

We estimate an expected intensity of dust emission in 850μm, $S(850\mu\mathrm{m})$, and a flux of molecular CO(6-5) line, $S(\mathrm{CO})$, assuming typical parameters of local starbursts. We start the calculations from our lower-limit of SFR, $34 M_\odot \mathrm{yr}^{-1}$. The far-infrared luminosity, $L(\mathrm{FIR})$, is calculated from $SFR[M_\odot \mathrm{yr}^{-1}] = 1.7 \times 10^{-10} L(\mathrm{FIR})[L_\odot]$ (Kennicutt 1998). We obtain $L(\mathrm{FIR}) = 2.0 \times 10^{11} L_\odot$. Assuming the modified blackbody radiation with a dust emissivity index of $\beta = 1.3$ and a dust temperature of $T_{\mathrm{dust}} = 35.6$ K (Dunne et al. 2000), we estimate the 850μm dust emission from $L(\mathrm{FIR})$ to be $S(850\mu\mathrm{m}) = 0.28$ mJy (see, e.g., Ouchi et al. 1999). This moderately bright 850μm emission is expected because of the negative k-correction (Blain et al. 2002). Again from the $L(\mathrm{FIR})$ value with the same modified blackbody radiation, the dust mass is $M_{\mathrm{dust}} = 6.0 \times 10^7 M_\odot$ via the relation presented in De Breuck et al. (2003). The mass of molecular hydrogen is $M(H_2) = 3.0 \times 10^9 M_\odot$

which is calculated with the relation of $M(\mathrm{H_2})/M_{\mathrm{dust}} = 50$ ($\sim 25-75$; Seaquist et al. 2004; Young et al. 1996). Finally, the flux of molecular CO(6-5) line is $S(\mathrm{CO}) = 0.1$ Jy km s^{-1} with the assumptions of an $\mathrm{H_2}$-to-CO conversion factor of 0.8 (Downes & Solomon 1998), and a line ratio of $\mathrm{CO}(6-5)/\mathrm{CO}(1-0) = 0.5$ (Bayet et al. 2006). In summary, we expect $S(850\mu\mathrm{m}) \gtrsim 0.28$ mJy and $S(\mathrm{CO}) \gtrsim 0.1$ Jy km s^{-1}, considering that our SFR is the lower limit ($> 34 M_{\odot}\mathrm{yr}^{-1}$). We use ALMA Sensitivity Calculator [7], and estimate the on-source integration time to be $\lesssim 0.2$ and $\lesssim 3$ hours for 5σ detections of a 850μm continuum and a CO(6-5) line, respectively. Here we assume the large beam size of $1''$ in a compact configuration of 50 12m-arrays for the point-source detection, the band width of 16 GHz, and the CO-line width of 250 km s^{-1} (Nishiyama & Nakai 2001) with a 50 km s^{-1} spectral resolution. Either of an 850μm-thermal continuum or a molecular-CO(6-5) line may be detected in reasonable observing time under the assumptions of local starbursts. If our object does not have dust or molecular gas as much as the local starbursts, a deficit of dust or molecular-line emission would be identified by ALMA observations. In either case, dust and molecular-gas properties of our object could be characterized in a few years.

We are grateful to Robert Antonucci, George Becker, Arjun Dey, Richard Ellis, Masakazu Kobayashi, Juna Kollmeier, Ivo Labbé, Janice Lee, Yuichi Matsuda, Kazuaki Ota, and Ann Zabludoff for their useful comments and discussions. We acknowledge Yuichi Matsuda for providing us the cutout narrow-band images of their Lyα blobs. We thank Michael Cooper who gave us helpful advices on the installation and the parameter choice of the spec2d pipeline. M.O. has been supported via Carnegie Fellowship. C.L.M. thanks the Packard Foundation for their financial support. This work is based in part on observations made with the Spitzer Space Telescope, which is operated by the Jet Propulsion Laboratory, California Institute of Technology under a contract with NASA. Support for this work was provided by NASA through an award issued by JPL/Caltech. This work is supported in part by Department of Energy contract DE-AC02-76SF00515. The authors wish to recognize and acknowledge the very significant cultural role and reverence that the summit of Mauna Kea has always had within the indigenous Hawaiian community. We are most fortunate to have the opportunity to conduct observations from this mountain.

Facilities: Subaru (Suprime-Cam), Keck:II (DEIMOS), Magellan:Baade (IMACS), Spitzer (IRAC,MIPS),

---

[7] http://www.eso.org/sci/facilities/alma/observing/tools/etc/index.html

REFERENCES

Basu-Zych, A., & Scharf, C. 2004, ApJ, 615, L85

Bayet, E., Gerin, M., Phillips, T. G., & Contursi, A. 2006, A&A, 460, 467

Bertin, E. & Arnouts, S. 1996, A&AS, 117, 393

Blain, A. W., Smail, I., Ivison, R. J., Kneib, J.-P., & Frayer, D. T. 2002, Phys. Rep., 369, 111

Brocklehurst, M. 1971, MNRAS, 153, 471

Bouché, N., Lehnert, M. D., Aguirre, A., Péroux, C., & Bergeron, J. 2007, MNRAS, 378, 525

Bouwens, R. J., Illingworth, G. D., Franx, M., & Ford, H. 2008, ArXiv e-prints, 803, arXiv:0803.0548

Bower, R. G., et al. 2004, MNRAS, 351, 63

Bruzual, G., & Charlot, S. 2003, MNRAS, 344, 1000

Calzetti, D., Armus, L., Bohlin, R. C., Kinney, A. L., Koornneef, J., & Storchi-Bergmann, T. 2000, ApJ, 533, 682

Castro Cerón, J. M., Michałowski, M. J., Hjorth, J., Malesani, D., Gorosabel, J., Watson, D., & Fynbo, J. P. U. 2008, ArXiv e-prints, 803, arXiv:0803.2235

Chapman, S. C., Scott, D., Windhorst, R. A., Frayer, D. T., Borys, C., Lewis, G. F., & Ivison, R. J. 2004, ApJ, 606, 85

Chary, R.-R., Teplitz, H. I., Dickinson, M. E., Koo, D. C., Le Floc'h, E., Marcillac, D., Papovich, C., & Stern, D. 2007, ApJ, 665, 257

Cowie, L. L., Songaila, A., Hu, E. M., & Cohen, J. G. 1996, AJ, 112, 839

De Breuck, C., et al. 2003, A&A, 401, 911

Dey, A., et al. 2005, ApJ, 629, 654

Dijkstra, M., Lidz, A., & Wyithe, J. S. B. 2007, MNRAS, 377, 1175

Dijkstra, M., Wyithe, J. S. B., & Haiman, Z. 2007, MNRAS, 379, 253

Dijkstra, M., & Loeb, A. 2008, ArXiv e-prints, 807, arXiv:0807.2645

Downes, D., & Solomon, P. M. 1998, ApJ, 507, 615

Drory, N., & Alvarez, M. 2008, ApJ, 680, 41

Dunlop, J. S., Cirasuolo, M., & McLure, R. J. 2007, MNRAS, 376, 1054

Dunne, L., Eales, S., Edmunds, M., Ivison, R., Alexander, P., & Clements, D. L. 2000, MNRAS, 315, 115

Egami, E., et al. 2005, ApJ, 618, L5

Eugenio Barrio, F., et al. 2008, ArXiv e-prints, 806, arXiv:0806.3688

Eyles, L. P., Bunker, A. J., Ellis, R. S., Lacy, M., Stanway, E. R., Stark, D. P., & Chiu, K. 2007, MNRAS, 374, 910

Fan, X., et al. 2006, AJ, 132, 117

Fardal, M. A., Katz, N., Gardner, J. P., Hernquist, L., Weinberg, D. H., & Davé, R. 2001, ApJ, 562, 605

Finkelstein, S. L., Rhoads, J. E., Malhotra, S., & Grogin, N. 2008, ArXiv e-prints, 806, arXiv:0806.3269

Furusawa, H., et al. 2008, ApJS, 176, 1

Gawiser, E., et al. 2007, ApJ, 671, 278

Geach, J. E., Smail, I., Chapman, S. C., Alexander, D. M., Blain, A. W., Stott, J. P., & Ivison, R. J. 2007, ApJ, 655, L9

Haiman, Z., & Rees, M. J. 2001, ApJ, 556, 87

Hayashino, T., et al. 2003, Publications of the National Astronomical Observatory of Japan, 7, 33

Hennawi, J. F., Prochaska, J. X., Kollmeier, J., & Zheng, Z. 2008, ArXiv e-prints, 807, arXiv:0807.2271

Iliev, I. T., Mellema, G., Pen, U.-L., Merz, H., Shapiro, P. R., & Alvarez, M. A. 2006, MNRAS, 369, 1625

Iye, M., et al. 2006, Nature, 443, 186

Kashikawa, N., et al. 2006, ApJ, 648, 7

Kennicutt, R. C., Jr. 1998, ApJ, 498, 541

Kobayashi, M. A. R., Totani, T., & Nagashima, M. 2007, ApJ, 670, 919

Komatsu, E., et al. 2008, ArXiv e-prints, 803, arXiv:0803.0547

Kriek, M., et al. 2006, ApJ, 649, L71

Labbé, I., et al. 2005, ApJ, 624, L81

Labbé, I., Bouwens, R., Illingworth, G. D., & Franx, M. 2006, ApJ, 649, L67

Lai, K., Huang, J.-S., Fazio, G., Cowie, L. L., Hu, E. M., & Kakazu, Y. 2007, ApJ, 655, 704

Lai, K., et al. 2008, ApJ, 674, 70

Lawrence, A., et al. 2007, MNRAS, 379, 1599

Madau, P. 1995, ApJ, 441, 18

Madau, P., Pozzetti, L., & Dickinson, M. 1998, ApJ, 498, 106

Martin, C. L., Kobulnicky, H. A., & Heckman, T. M. 2002, ApJ, 574, 663

Matsuda, Y., et al. 2004, AJ, 128, 569

Matsuda, Y., Yamada, T., Hayashino, T., Yamauchi, R., & Nakamura, Y. 2006, ApJ, 640, L123

Matsuda, Y., Iono, D., Ohta, K., Yamada, T., Kawabe, R., Hayashino, T., Peck, A. B., & Petitpas, G. R. 2007, ApJ, 667, 667

McCarthy, P. J. 1993, ARA&A, 31, 639

McCarthy, P. J., Spinrad, H., Djorgovski, S., Strauss, M. A., van Breugel, W., & Liebert, J. 1987, ApJ, 319, L39

McLure, R. J., Cirasuolo, M., Dunlop, J. S., Foucaud, S., & Almaini, O. 2008, ArXiv e-prints, 805, arXiv:0805.1335

McQuinn, M., Hernquist, L., Zaldarriaga, M., & Dutta, S. 2007, MNRAS, 381, 75

Miyazaki, S., et al. 2002, PASJ, 54, 833

Mobasher, B., et al. 2005, ApJ, 635, 832

Mortier, A. M. J., et al. 2005, MNRAS, 363, 563

Nilsson, K. K., Fynbo, J. P. U., Møller, P., Sommer-Larsen, J., & Ledoux, C. 2006, A&A, 452, L23

Nilsson, K. K., et al. 2007, A&A, 471, 71

Nishiyama, K., & Nakai, N. 2001, PASJ, 53, 713

Ohyama, Y., et al. 2003, ApJ, 591, L9

Ota, K., et al. 2008, ApJ, 677, 12

Ouchi, M., Yamada, T., Kawai, H., & Ohta, K. 1999, ApJ, 517, L19

Ouchi, M., et al. 2004, ApJ, 611, 660

Ouchi, M., et al. 2008, ApJS, 176, 301

Peng, C. Y., Ho, L. C., Impey, C. D., & Rix, H.-W. 2002, AJ, 124, 266

Pettini, M., Smith, L. J., King, D. L., & Hunstead, R. W. 1997, ApJ, 486, 665

Pindor, B., et al. 2006, AJ, 131, 41

Pirzkal, N., Malhotra, S., Rhoads, J. E., & Xu, C. 2007, ApJ, 667, 49

Reuland, M., et al. 2003, ApJ, 592, 755

Sadat, R., Guiderdoni, B., & Silk, J. 2001, A&A, 369, 26

Saito, T., Shimasaku, K., Okamura, S., Ouchi, M., Akiyama, M., & Yoshida, M. 2006, ApJ, 648, 54

Saito, T., Shimasaku, K., Okamura, S., Ouchi, M., Akiyama, M., Yoshida, M., & Ueda, Y. 2008, ApJ, 675, 1076

Scannapieco, E., Schneider, R., & Ferrara, A. 2003, ApJ, 589, 35

Seaquist, E., Yao, L., Dunne, L., & Cameron, H. 2004, MNRAS, 349, 1428

Sheth, R. K. & Tormen, G. 1999, MNRAS, 308, 119

Simard, L., et al. 1999, ApJ, 519, 563

Simpson, C., et al. 2006, MNRAS, 372, 741

Smith, D. J. B., & Jarvis, M. J. 2007, MNRAS, 378, L49

Smith, D. J. B., Jarvis, M. J., Lacy, M., & Martínez-Sansigre, A. 2008, ArXiv e-prints, 806, arXiv:0806.4384

Stark, D. P., Ellis, R. S., Richard, J., Kneib, J.-P., Smith, G. P., & Santos, M. R. 2007, ApJ, 663, 10

Steidel, C. C., Adelberger, K. L., Shapley, A. E., Pettini, M., Dickinson, M., & Giavalisco, M. 2000, ApJ, 532, 170

Shimasaku, K., et al. 2006, PASJ, 58, 313

Taniguchi, Y., & Shioya, Y. 2000, ApJ, 532, L13

Taniguchi, Y., et al. 2005, PASJ, 57, 165

Tapken, C., Appenzeller, I., Noll, S., Richling, S., Heidt, J., Meinköhn, E., & Mehlert, D. 2007, A&A, 467, 63

Trac, H., & Cen, R. 2007, ApJ, 671, 1

Uchimoto, Y. K., et al. 2008, ArXiv e-prints, 802, arXiv:0802.3958

Ueda, Y., et al. 2008, ArXiv e-prints, 806, arXiv:0806.2846

van Breukelen, C., et al. 2006, MNRAS, 373, L26

van Ojik, R., Roettgering, H. J. A., Miley, G. K., & Hunstead, R. W. 1997, A&A, 317, 358

Weidinger, M., Møller, P., Fynbo, J. P. U., & Thomsen, B. 2005, A&A, 436, 825

Wilman, R. J., Gerssen, J., Bower, R. G., Morris, S. L., Bacon, R., de Zeeuw, P. T., & Davies, R. L. 2005, Nature, 436, 227

Yagi, M., Kashikawa, N., Sekiguchi, M., Doi, M., Yasuda, N., Shimasaku, K., & Okamura, S. 2002, AJ, 123, 66

Yan, H., & Windhorst, R. A. 2004, ApJ, 600, L1

Yan, H., et al. 2005, ApJ, 634, 109

Yan, H., Dickinson, M., Giavalisco, M., Stern, D., Eisenhardt, P. R. M., & Ferguson, H. C. 2006, ApJ, 651, 24

Yang, Y., Zabludoff, A. I., Davé, R., Eisenstein, D. J., Pinto, P. A., Katz, N., Weinberg, D. H., & Barton, E. J. 2006, ApJ, 640, 539

Young, J. S., Allen, L., Kenney, J. D. P., Lesser, A., & Rownd, B. 1996, AJ, 112, 1903

Table 1. Photometry of Himiko

Band	Mag(2″) (1)	Mag/Flux(Total) (2)
$f(0.5-2\text{keV})^2$	$\cdots$	$< 6 \times 10^{-16}$
B	> 28.7	> 27.9
V	> 28.2	> 27.4
R	> 28.1	> 27.3
i'	> 28.0	> 27.2
z'^3	25.86 ± 0.20	25.45 ± 0.27
$NB921^3$	23.91 ± 0.04	23.55 ± 0.05
$m_{0.95}$	25.74 ± 0.64	25.18 ± 0.73
J^4	24.95 ± 0.53	24.01 ± 0.43
H^4	> 24.7	> 24.0
K^4	24.42 ± 0.50	> 23.8
$m(3.6\mu\text{m})$	$\cdots$	24.02 ± 0.27
$m(4.5\mu\text{m})$	$\cdots$	> 23.9
$m(5.8\mu\text{m})$	$\cdots$	> 22.0
$m(8.0\mu\text{m})$	$\cdots$	> 21.8
$m(24\mu\text{m})$	$\cdots$	> 19.8
$S(850\mu m)$	$\cdots$	$< 12\text{mJy}$
$f(1.4\text{GHz})$	$\cdots$	$< 100\mu\text{Jy}$

Note. — Col.(1): The 2″-diameter aperture magnitude. Col.(2): The total magnitude or flux. In these two columns, the upper limits are 2σ and 3σ magnitudes in $B-K$ and $3.6-24\mu$m bands, respectively.

[2] In units of erg cm^{-2} s^{-1}.

[3] Isophotal magnitudes are 25.67 ± 0.21 and 23.66 ± 0.04 in z' and $NB921$ bands, respectively.

[4] Magnitudes in J and K bands are slightly over the 2σ level. However, neither of them are detected beyond the 3σ level.

Table 2. Properties of Himiko

Quantity	Measurement
Redshift(z)	6.595
Skewness of Lyα (S)	0.685 ± 0.007
Weighted Skewness of Lyα (S_w)	13.2 ± 0.1
Isophotal Area[1] ($NB921$)	5.22 arcsec^2
Isophotal Area[1] (z')	1.88 arcsec^2
Major Axis[2] ($NB921$)	$3.1''$
Major Axis[2] (z')	$2.0''$
Lyα Surface Brightness	1.51×10^{-17} erg s^{-1} cm^{-2} arcsec^{-2}
$NB921$ Surface Brightness	25.5 mag arcsec^{-2}
f(Lyα)[3]	$7.9 \pm 0.5 \times 10^{-17}$ erg s^{-1} cm^{-2}
L(Lyα)[3]	$3.9 \pm 0.2 \times 10^{43}$ erg s^{-1}
$M(1250)$[4]	-21.67 ± 0.73 mag
M_B[4]	-22.83 ± 0.27 mag
Lyα Line Width (FWHM)	251 ± 21 km s^{-1}
Rest-Frame Equivalent Width (EW_0)	100^{+302}_{-43} Å
Stellar Mass	$3.5^{+1.5}_{-2.6} \times 10^{10} M_\odot$
SFR from SED fit[5]	$> 34 M_\odot \mathrm{yr}^{-1}$
SFR from UV[5]	$25^{+24}_{-12} M_\odot$ yr^{-1}
SFR from Lyα[5]	$36 \pm 2 M_\odot$ yr^{-1}
Specific SFR	$> 1.6 \times 10^{-9} \mathrm{yr}^{-1}$
Number Density[6]	1.2×10^{-6} Mpc^{-3}

[1] The isophotal areas are defined as pixels with values above the 2σ sky fluctuation; 26.8 and 27.3 mag arcsec^{-2} in the $NB921$ and z' images, respectively.

[2] The maximum size of the 2σ isophotal area. For isophotal areas above the 3σ sky fluctuation, we obtain $2''.7$ and $1''.2$ in the $NB921$ and z' images, respectively.

[3] The Lyα flux and luminosity from the photometric measurements.

[4] The rest-frame 1250Å, $M(1250)$, and B-band, M_B, magnitudes. Since the 3.6μm band observes the rest-frame 4180-5168Å which is very close to the bandpass of B band, no k-correction is applied to the 3.6μm-band magnitude.

[5] The SFRs estimated from the SED fitting, the UV continuum, and the Lyα luminosity. The SFRs of UV and Lyα are not corrected for dust extinction. See §3.4 for more details.

[6] The comoving number density corresponding to Himiko.

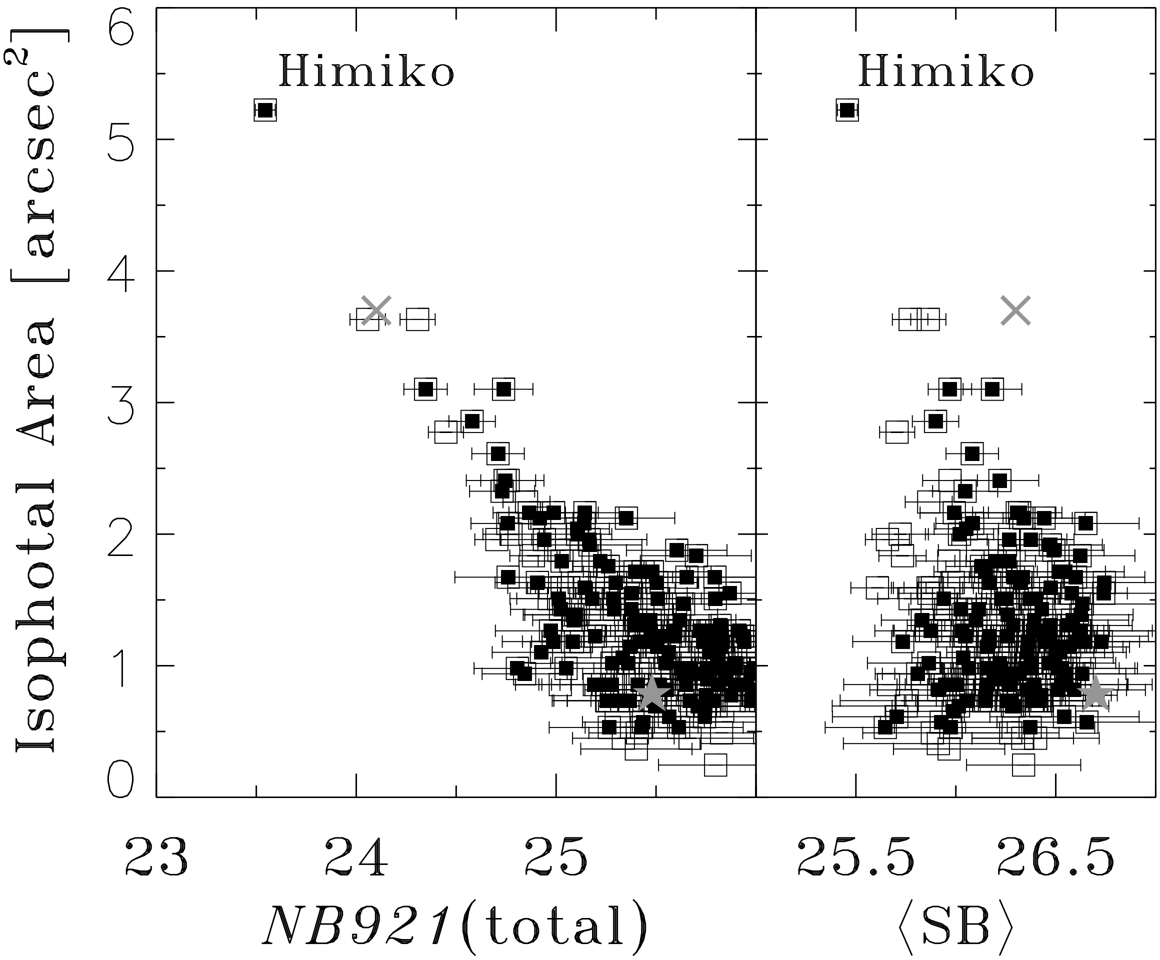

Fig. 1.— Isophotal area of our $z = 6.6$ LAE candidates as a function of total $NB921$ magnitude (left panel) and average $NB921$ surface brightness, $\langle SB \rangle$ (right panel). $\langle SB \rangle$ is expressed in units of mag arcsec^{-2}. The square with a label of Himiko is our giant LAE. The open squares with a filled square represent $z = 6.6$ LAE candidates showing a possibly extended profile with a FWHM of $> 1''.2$ in the $NB921$ image, while the simple open squares indicate the other (FWHM$\leq 1''.2$) candidates. The measurements of FWHM include large uncertainties for faint sources with $NB921 \simeq 25 - 26$, and become unreliable in this faint magnitude regime. The gray star and cross marks denote our simulated blob 1 and 28, respectively (see §4.1).

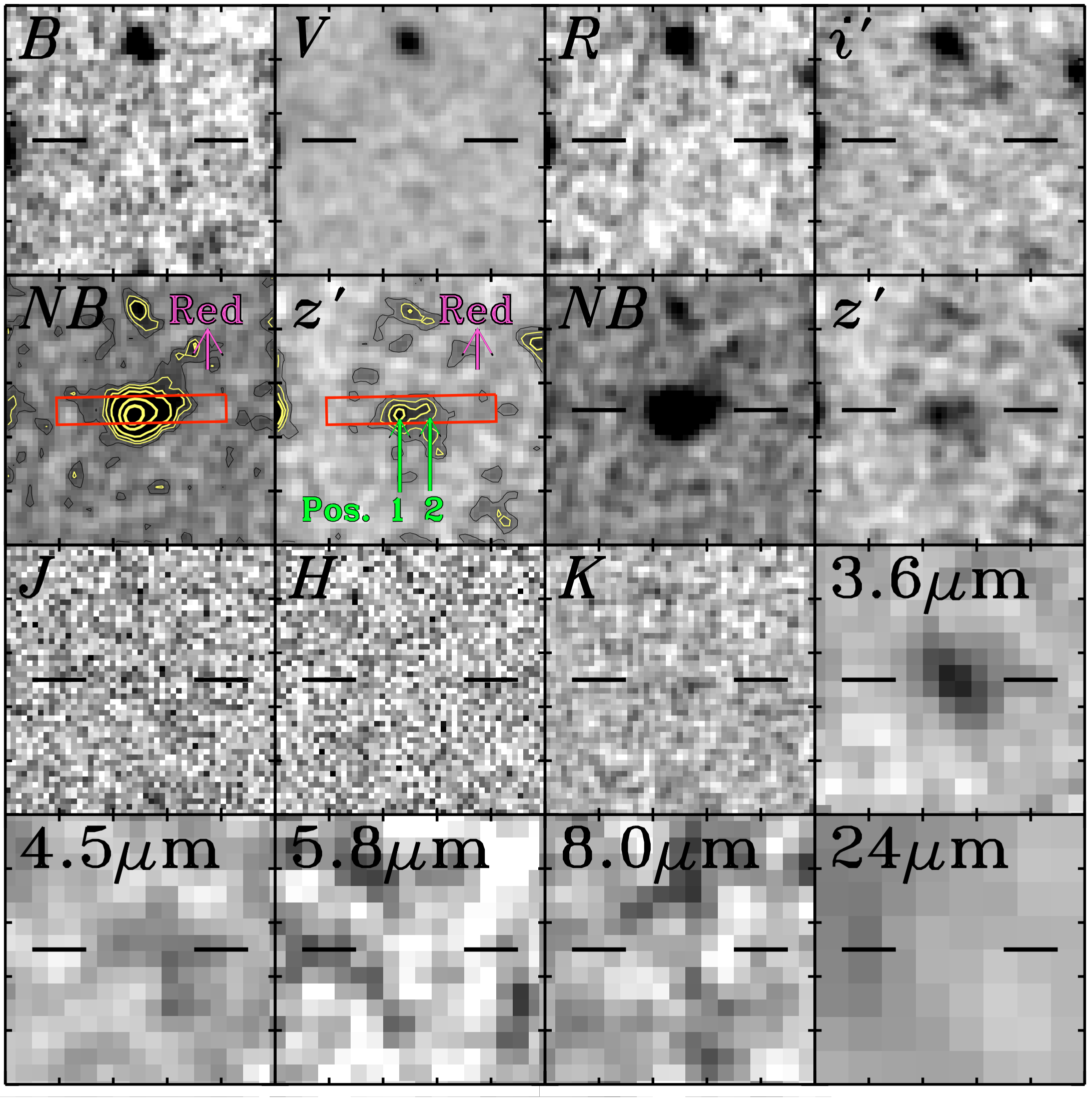

Fig. 2.— Optical to infrared images of Himiko. North is up and east is to the left. We display $10'' \times 10''$ images at $BVRi'z'$ and NB ($NB921$) bands from Subaru/SXDS, at JHK bands from UKIDSS-UDS DR3, and $3.6-24\mu$m bands from Spitzer/SpUDS. We show intensity contours in $NB921$ and z' images. The black contours denote 1 σ level of sky fluctuation. The yellow contours represent (2, 3, 5, 10, 15) and (2,3,4) σ levels of sky fluctuations in $NB921$ and z' images, respectively. We also plot the position of the DEIMOS slit by the red box. The dispersion direction towards red spectrum is shown by the magenta arrow. The green arrows point to the *position* 1 and 2 that are probable peaks in the z' image.

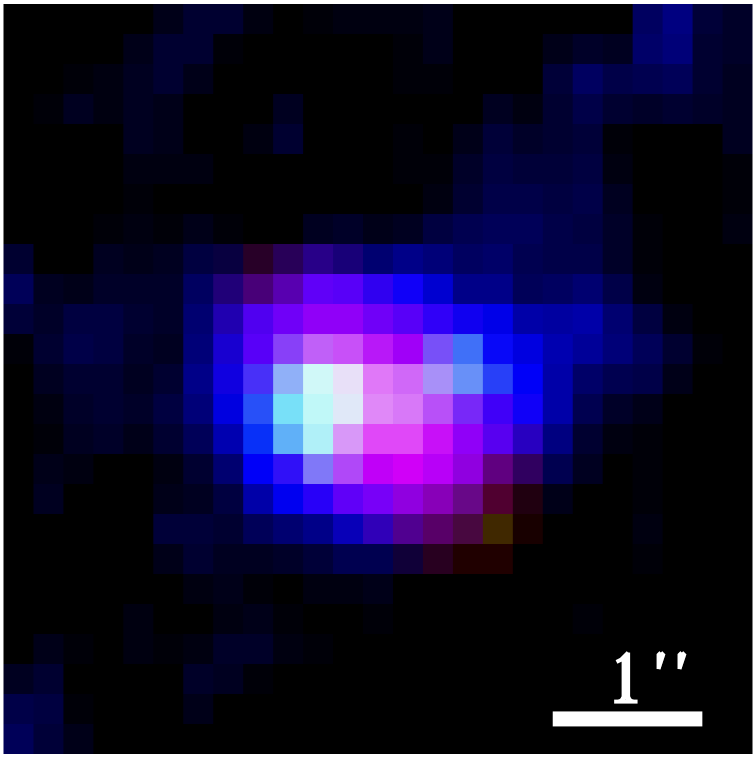

Fig. 3.— Composite pseudo-color image of Himiko. The RGB colors are assigned to 3.6μm , z', and $NB921$ images, respectively. North is up and east is to the left. The image size is $5'' \times 5''$. The white bar at the bottom right represents the length of one arcsecond. The brightest peak with a bluish white color corresponds to *position* 1. The *position* 2 is located 1.1 arcsec west of the *position* 1.

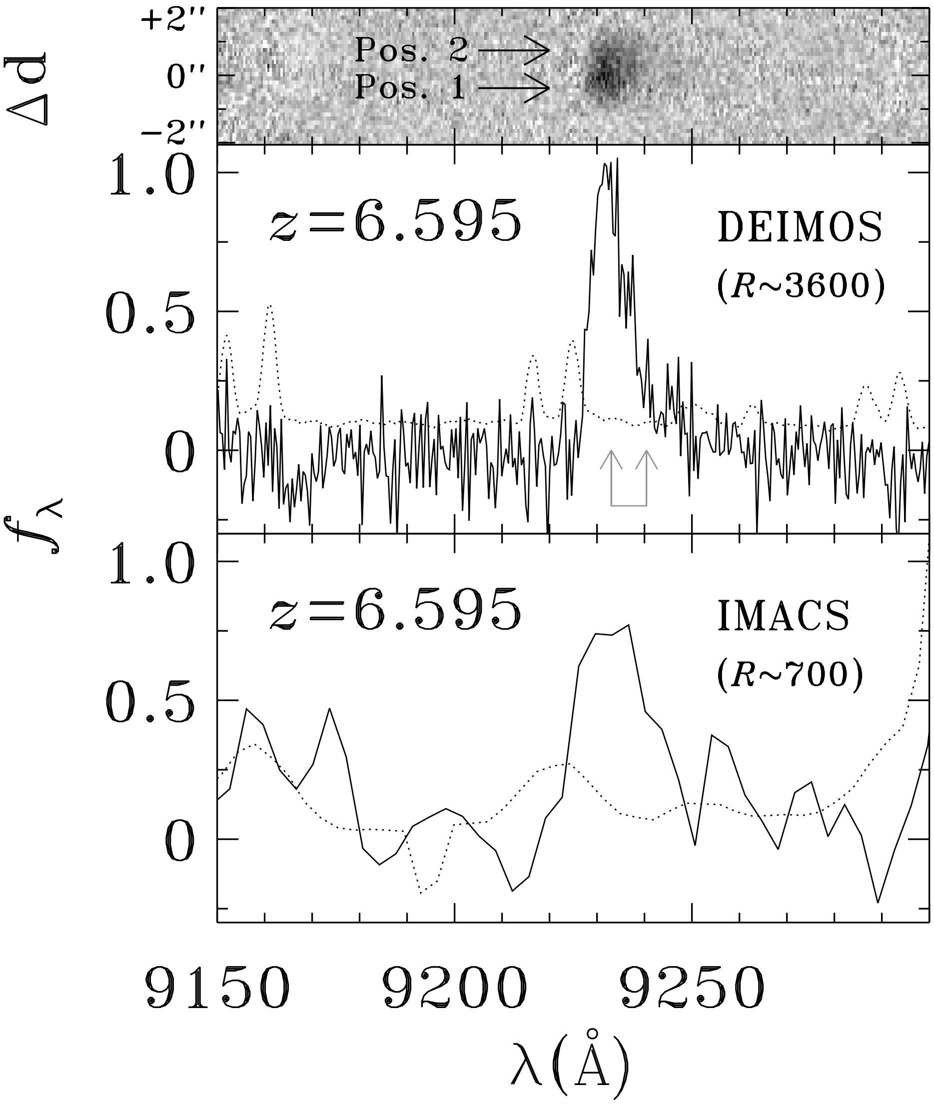

Fig. 4.— Spectra of the giant LAE, Himiko. The top panel shows the two-dimensional spectrum obtained from DEIMOS observations. The horizontal arrows point to the *position* 1 and 2. The middle and bottom panels present the spectra taken with DEIMOS and IMACS, respectively. We show spectra of the giant LAE (solid line) and the background sky (dotted line). The units of the vertical axis are in 10^{-17} erg s^{-1} cm^{-2} $Å^{-1}$ in the bottom panel (IMACS), and arbitrary in the middle panel (DEIMOS). Two vertical arrows in the middle panel indicate the wavelengths of [O II] $\lambda\lambda$3726,3729 doublet from a $z = 1.5$ [O II] emitter.

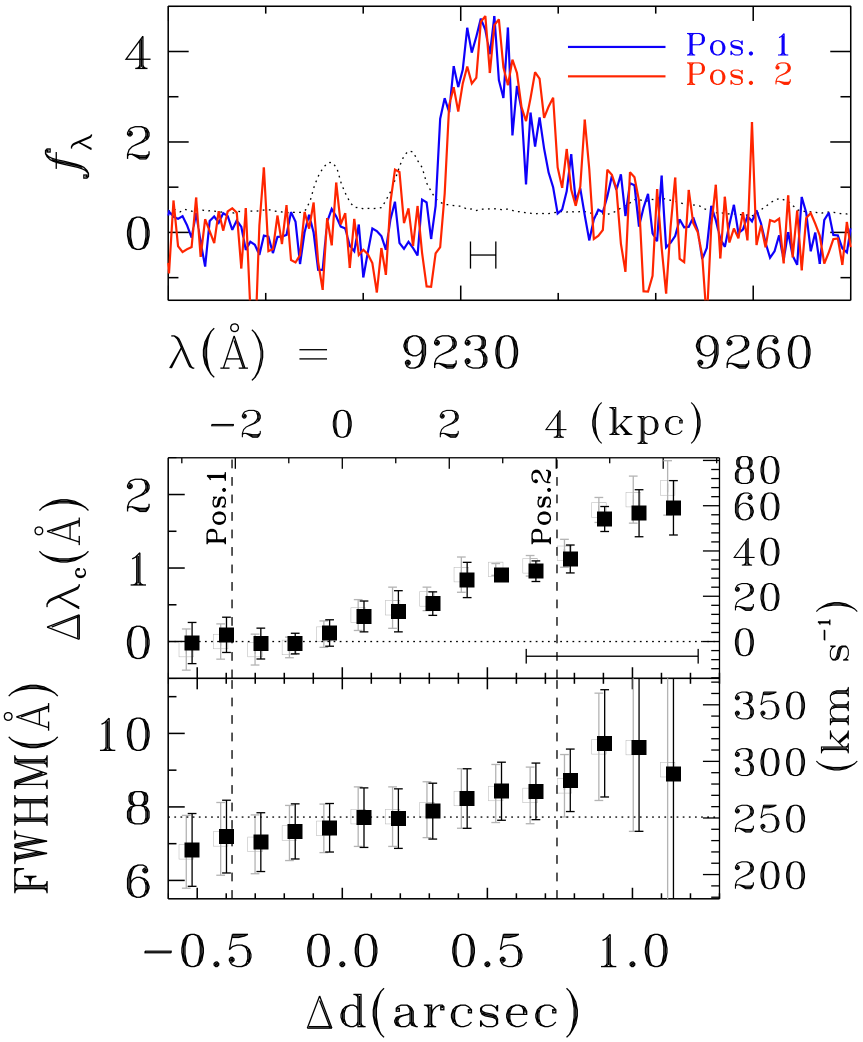

Fig. 5.— *Top*: DEIMOS spectra at *position* 1 (blue) and 2 (red). The dotted line represents the background sky. The instrumental FWHM is indicated with the bar below the emission line. *Bottom*: The line-center offset (upper panel) and FWHM line width (lower panel) as a function of position. The $\Delta\lambda_c$ is defined by $\Delta\lambda_c = \lambda_c - \lambda_c(\Delta d = 0)$, where λ_c is the line-center wavelength. The definition of Δd is the same as that of the top panel in Figure 4, and $\Delta d = 0$ corresponds to the Lyα source center. The gray open squares are the direct measurements, while the black squares are the best estimates after the correction (see the text). The size of spatial binning (0".6) is shown with the bar on the right side. The dotted lines present the values at $\Delta d = 0$. The *positions* of 1 and 2 are indicated with the dashed lines. The right-hand vertical axis ticks the corresponding velocity. The FWHM-line width is corrected for the instrumental broadening with the assumption of a Gaussian profile.

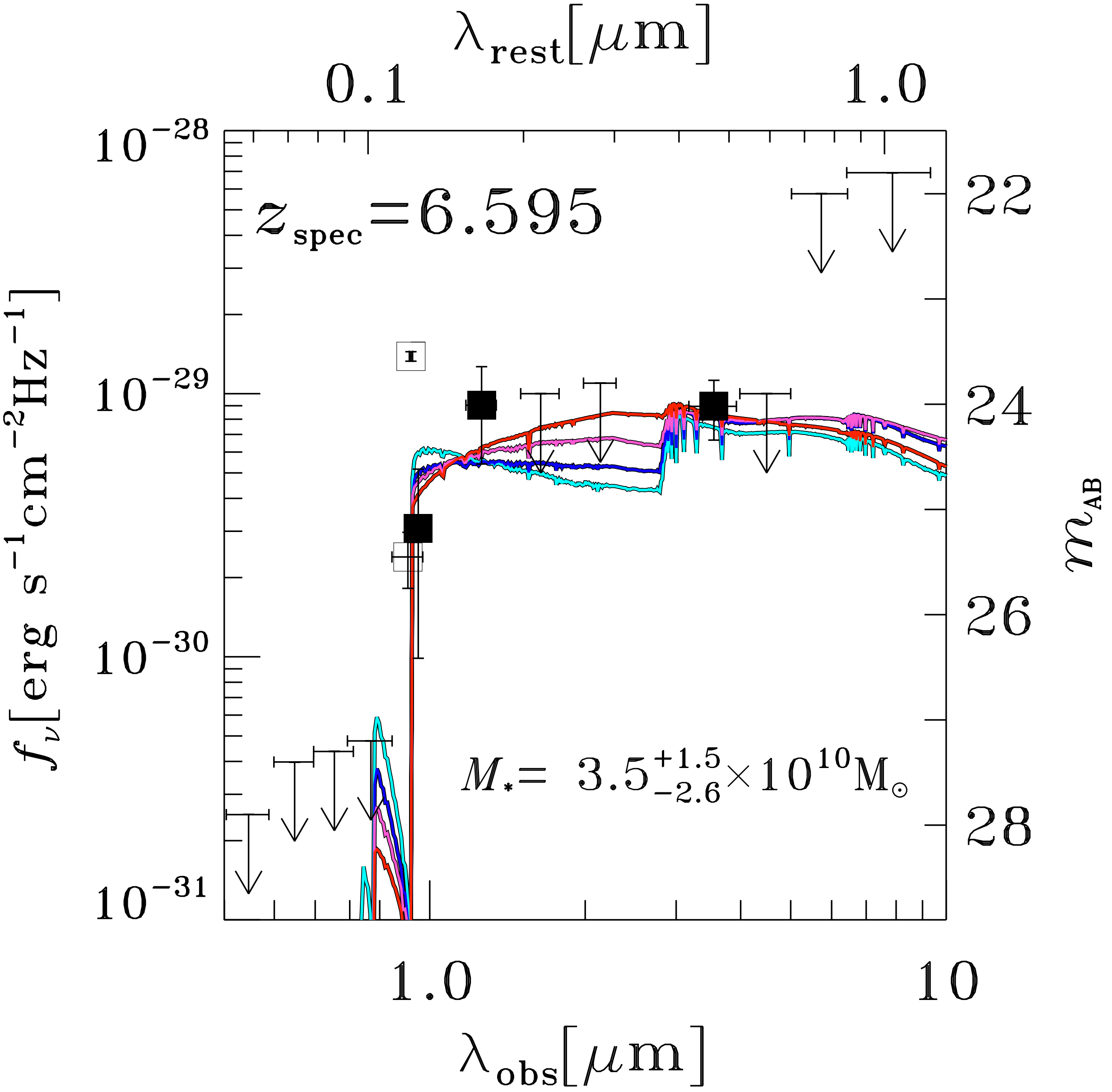

Fig. 6.— Spectral energy distribution (SED) of the giant LAE, Himiko. The squares represent the total fluxes of this object taken from Table 1. The open symbols are data points that are not used for the SED fitting, since these bands are contaminated by the strong Lyα emission line. The cyan, blue, magenta, and red lines show the best-fit stellar synthesis models with $E(B-V) = 0.0$, 0.3, 0.6, 0.9, respectively, under the assumptions of constant star formation with a fixed metallicity of $Z = 0.02Z_{\odot}$.

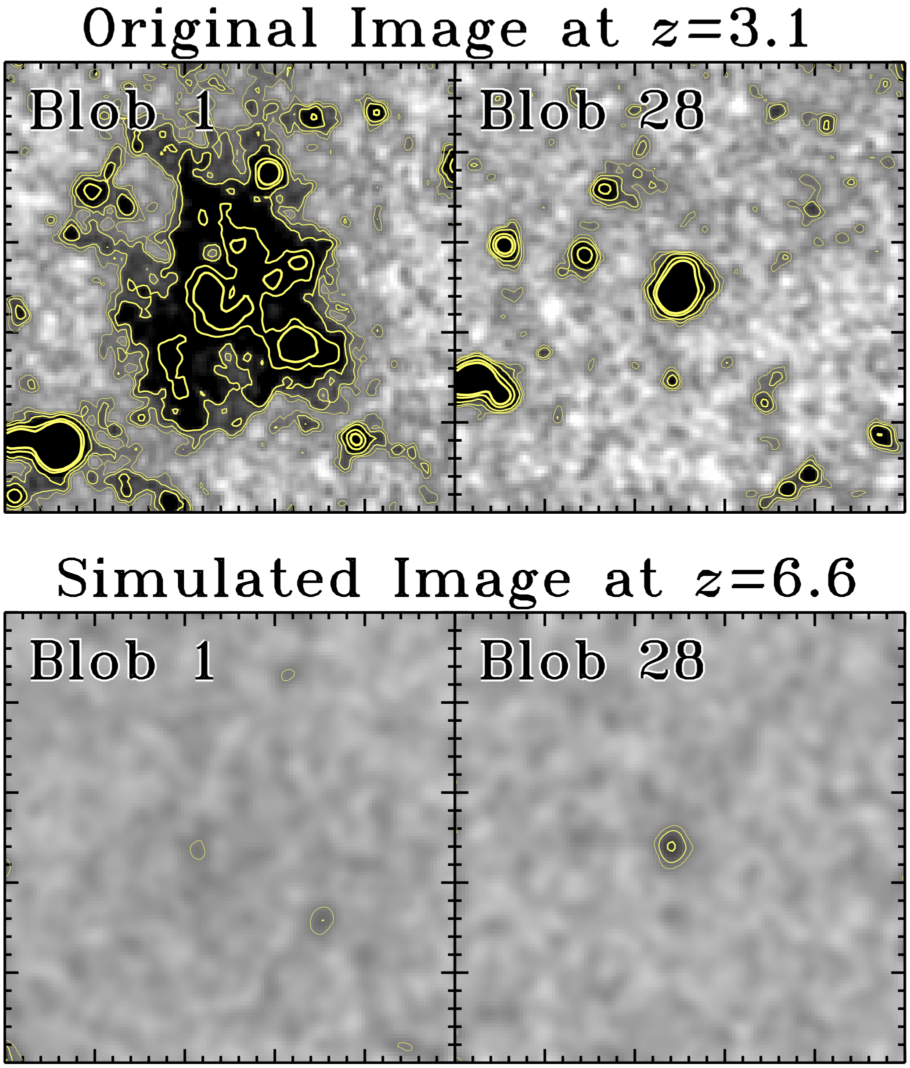

Fig. 7.— Original narrow-band images of blob 1 and 28 at $z = 3.1$ from Matsuda et al. (2004) (top panels) and simulated narrow-band images at $z = 6.6$ (bottom panels). The size of each panel is $25'' \times 25''$. The intensity contours are presented with yellow lines. The contours represent (2, 3, 5, 10, 15) σ levels of sky fluctuations, where the 2σ sky fluctuations correspond to 28.0 and 26.8 mag arcsec^{-2} in the original images (Matsuda et al. 2004) and the simulated images, respectively. Note that the absolute values of contour levels in the simulated images are the same as the yellow contours in the $NB921$ image of Figure 2. In the original images, blob 1 is the large diffuse extended source, while blob 28 is the compact source at the center. Note that the original and simulated images include foreground and background sources neighboring the blobs in the $25'' \times 25''$ areas.